THE JOURNAL OF PHYSICAL CHEMISTRY C

Article

pubs.acs.org/JPCC

Phase Transitions and Polymerization of $C_6H_6{-}C_6F_6$ Cocrystal under Extreme Conditions

Yajie Wang,[†] Lijuan Wang,[†] Haiyan Zheng,[*,†] Kuo Li,[*,†] Michał Andrzejewski,[‡] Takanori Hattori,[§] Asami Sano-Furukawa,[§] Andrzej Katrusiak,[‡] Yufei Meng,[†] Fuhui Liao,[∥] Fang Hong,[†] and Ho-kwang Mao[†,⊥,#]

[†]Center for High Pressure Science and Technology Advanced Research, Beijing 100094, P. R. China

[‡]Faculty of Chemistry, Adam Mickiewicz University, Umultowska 89b, 61-614 Poznan, Poland

[§]J-PARC Center, Japan Atomic Energy Agency, Tokai, Ibaraki 319-1195, Japan

[∥]College of Chemistry and Molecular Engineering, Peking University, Beijing 100871, P. R. China

[⊥]HPSynC, Geophysical Laboratory, Carnegie Institution of Washington, Argonne, Illinois 60439, United States

[#]Geophysical Laboratory, Carnegie Institution of Washington, Washington, DC 20015, United States

Supporting Information

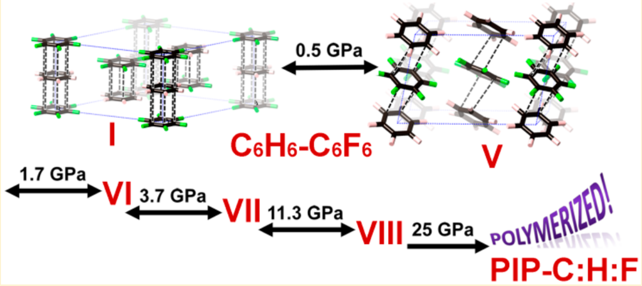

ABSTRACT: Pressure-induced polymerization (PIP) of aromatic molecules can generate saturated carbon nanostructures. As a strongly interacted $\pi-\pi$ stacking unit, the $C_6H_6-C_6F_6$ adduct is widely applied in supramolecular chemistry, and it provides a good preorganization for the PIP. Here we investigated the structural variation of $C_6H_6-C_6F_6$ cocrystal and the subsequent PIP process under high pressure. Four new molecular-complex phases V, VI, VII, and VIII have been identified and characterized by the in situ Raman, IR, synchrotron X-ray, and neutron diffraction. The phase V is different from the phases observed at low temperature, which has a tilted column structure. Phases VI and VII have a structure similar to phase V. Phase VIII polymerizes irreversibly upon compression above 25 GPa without any catalyst, producing $sp^3(CH/F)_n$ materials. The $\pi-\pi$ interaction is still dominant below 0.5 GPa but is most likely to be overstepped under further compression, which is important for discussing the supramolecular phase transition and the polymerization process.

■ INTRODUCTION

Carbon materials including the fullerene, nanotube, graphene, and diamond continue to gain more and more attention due to their extraordinary electronic and mechanical properties.[1−3] Pressure-induced polymerization (PIP) has been evidenced as an effective tool for synthesizing functional carbon materials.[4−7] Under high pressure, the unsaturated molecules tend to form more saturated polymer with extended structure and higher density.[8−11] Benzene, as the prototypic model of aromatic compounds, was extensively studied both theoretically and experimentally under various temperature, pressure, and irradiation conditions. Three crystalline phases were discovered and characterized by spectroscopic and X-ray diffraction investigations under high pressure, and amorphous hydrogenated carbon was produced when compressed to 30 GPa.[12−16] The structure of the product and the reaction path were investigated theoretically, and several models constructed by $C(sp^3)$:H were proposed.[14−20] Recently, by optimizing the synthetic conditions, crystalline 1D sp^3 carbon nanothread (hereafter referred as PIP-B) was identified from the sample recovered from compressed benzene at room temperature.[21] Compared with traditional sp^2 nanotubes, higher strength and stiffness were expected for this diamond-type nanothread. This high-pressure synthetic method opens a new route to construct ordered carbon nanomaterials. Modified products with other functional groups toward particular properties are hence expected.

Interaction between benzene (C_6H_6) and hexafluorobenzene (C_6F_6) has been studied since the 1960s.[22] C_6H_6 and C_6F_6 form a 1:1 cocrystal that has the melting point at 297 K, higher than those of the neat constituents by 20 K.[23] In benzene, the hydrogen atoms are electron-deficient, and the carbon ring is electron-rich, while on hexafluorobenzene the charge distribution is just the opposite. This results in strong electrostatic attraction between the parallel stacked $C_6H_6-C_6F_6$ rings and makes this complex an important building block in crystal engineering and supramolecular chemistry. Four crystalline phases of the $C_6H_6-C_6F_6$ cocrystal have been identified at low

Received: November 8, 2016
Revised: December 1, 2016
Published: December 1, 2016

DOI: 10.1021/acs.jpcc.6b11245
J. Phys. Chem. C 2016, 120, 29510−29519

temperature, namely, phases I [R-3m], II [$I2/m$], III [P-1], and IV [$P2_1/a$],[24,25] all of them adopting the alternating stacking. For the PIP synthesis, this preorganized column structure may help to direct the polymerization and generate ordered carbon nanostructure. Most importantly, the strongly electronegative fluorine atoms are expected to affect the reaction path and properties of the product.[26] The obtained fluorinated carbon material may have superhydrophobic and optoelectronic properties.[27,28] However, to our knowledge, the behavior of benzene-hexafluorobenzene cocrystal (C_6H_6–C_6F_6) was only investigated under low temperature.[24,25] The responses under high pressure are still unknown, and the effects of fluorine substitution on the PIP reaction and the properties of the obtained polymer are still awaiting investigation.

We investigated the phase transitions and polymerization of C_6H_6–C_6F_6 cocrystal under high pressure at room temperature using in situ Raman, IR spectra, X-ray diffraction (XRD), and neutron diffraction techniques. Four transitions between molecular phases and a polymerization were identified, and their structures were investigated. The crystal structures of high-pressure phases (V–VIII) are different from those of low-temperature phases (II–IV). The complex phase relationship of C_6H_6–C_6F_6 cocrystal under high pressure and low temperature is described. The variations of the vibration modes and their relationships to the local structure under compression are discussed.

■ EXPERIMENTAL METHODS

Benzene (99.9%) and hexafluorobenzene (99.9%) were purchased from Sigma-Aldrich and used without further purification. The C_6H_6–C_6F_6 cocrystal was prepared by mixing equimolar amounts of C_6H_6 and C_6F_6. For the in situ Raman, IR, and powder XRD experiments, a symmetric diamond anvil cell (DAC) with an anvil culet size of 300 um in diameter was used. The type-IIa diamond anvils were used for IR experiment to avoid absorption band at 1300–1000 cm^{-1}. T-301 stainless-steel gaskets were preindented to ~30 um in thickness and center holes with d = 100 um were drilled to serve as a sample chamber. The pressure was determined by measuring the ruby fluorescence, according to the equation P (GPa) = 248.4[$(\lambda/\lambda_0)^{7.665} - 1$].[29]

Raman experiments were carried out on a Renishaw Raman microscope (RM1000). The 532 nm line of a Nd:YAG laser was used as the excitation source. The system was calibrated by the Si line. Because of the cutoff of the notch filter, the measurable Raman spectral range is above 60 cm^{-1}. IR experiments were performed on a Bruker VERTEX 70v with HYPERION 2000 microscope. A Globar was used as a conventional source. The spectra were collected in transmission mode in the range of 600–4000 cm^{-1} with a resolution of 4 cm^{-1} through a 20 × 20 μm^2 aperture. The diamond anvil absorption in the aperture region was used as the background. The synchrotron XRD data were collected at beamline 12.2.2, Advanced Light Source (ALS), Lawrence Berkeley National Lab (LBNL). The monochromated incident X-ray wavelength was 0.4973 Å. The preliminary data reduction was performed using the Dioptas program.[30] To prepare good powder sample, the C_6H_6–C_6F_6 cocrystal was loaded in the DAC under liquid nitrogen temperature and sealed quickly to avoid the possible formation of big grains or preferred orientation. The in situ high-pressure neutron diffraction was measured in J-PARC BL11 (PLANET).[31] A Paris-Edinburgh press VX4 was used to provide a maximum pressure of 20 GPa at room temperature. Single toroidal WC anvils were used for experiments below 10 GPa, and sintered diamond double toroidal anvils were used for experiments above 10 GPa. Ti–Zr alloy gaskets were used as the sample chamber. The pressure was calculated using the calibration curve of the instrument. The collection at one pressure point lasted over 8 h. The compressing and decompressing rate was kept at 1 bar/min (~0.1 GPa/min).

The single-crystal X-ray diffraction data were collected using a KUMA KM-4 CCD diffractometer with graphite mono-chromated Mo K$_\alpha$ radiation. The centering of the DAC was performed by the gasket-shadowing method.[32] The reflections were collected with the ω-scans technique, 0.7° frame widths, and 35 s exposures. Program suite CrysAlis was used for data collections, determination of the UB matrices, initial data reductions, and Lp corrections. In all of the measurements, the reflection intensities have been corrected for the effects of absorption of X-rays by the DAC, shadowing of the beams by the gasket edges, and absorption of the sample crystals themselves.

The low-temperature X-ray diffraction data were collected using a Bruker D8 diffractometer working with the Cu K$_\alpha$ radiation (λ = 1.5418 Å), with the step of 0.02° and the step duration of 10 s. The sample was frozen on the sample stage at −53 °C, and the sample chamber was then evacuated. The data were collected and the temperature was then increased for more data points.

■ RESULTS AND DISCUSSION

Raman Spectra of C_6H_6–C_6F_6 Cocrystal under High Pressure. When compressing the C_6H_6–C_6F_6 sample slowly from 0.05 to 0.10 GPa, a visible liquid-to-solid transition was observed under optical microscope. The Raman peaks become sharper (Figure 1), and the lattice mode at 88 cm^{-1} and the peak at 375 cm^{-1} are strongly enhanced. The assignment of the Raman modes of C_6H_6–C_6F_6 cocrystal is shown in Table 1 based on the spectroscopic information reported at 77 K.[33] Most of the peaks in the range above 200 cm^{-1} are very similar to those of pure C_6F_6 or pure C_6H_6 indicating no strong interactions between C_6F_6 and C_6H_6 at this pressure, similarly as the situation at 0.1 MPa/77 K.[33] As discussed later, this is phase I of C_6H_6–C_6F_6 cocrystal.

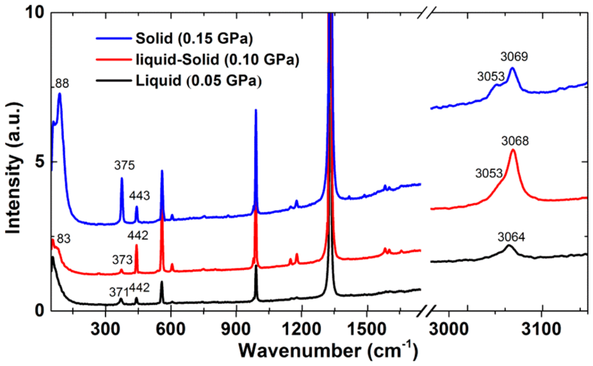

Figure 1. Raman spectra of C_6H_6–C_6F_6 complex in the solid state and the liquid state.

The evolution of Raman spectra lower than 300 cm^{-1} with increasing pressure is shown in Figure 2, which usually includes the lattice modes reflecting the intermolecular interactions. All of the modes show obvious blue shifts with increasing pressure. As displayed in Figure 2a, two new modes, marked by the

Table 1. Assignments of Raman modes of $C_6H_6{-}C_6F_6$ Complex at 77 K,[33] 1 atm, and 0.15 GPa, Room Temperature (RT)

77 K	0.15 GPa	assignments
267 vw		
375 s	375 s	ν_{10F} (C−F out-of-plane bending)
441 s	443 s	ν_{6F} (C−C−C in-plane bending)
558 vs	560 vs	ν_{1F} (Ring breathing)
604 s	606 w	ν_{6H} (C−C−C in-plane bending)
752 vw		$2\nu_{10F}$
852 m		ν_{10H}
980 m	981 w	$\nu_{1H}{}^1$ (ring breathing for $^{13}CC_5H_6$)
988 vvs	991 vvs	ν_{1H} (ring breathing)
1010 w		ν_{5H} (C−H bond out of plane vibration)
1146 vw		ν_{7F} (C−F stretching)
1152 w	1150 vw	ν_{7F} (C−F stretching)
1165 w		ν_{9H} (C−H in-plane bending)
1171 s		ν_{9H} (C−H in-plane bending)
1175 s		ν_{9H} (C−H in-plane bending)
1178 s	1178 w	ν_{9H} (C−H in-plane bending)
1582 vs	1584 w	ν_{8H} (C−H in-plane bending)
1601 s	1604 w	$\nu_{1H} + \nu_{6H}$
1660 vw	1660 vw	ν_{8F} (C−C stretching)
2923 vw		$\nu_{3H} + \nu_{8H}$
2942 w		$2\nu_{19H}$
2948 w		$2\nu_{19H}$
3041 m		ν_{7H} (doubly degenerate C−H stretching)
3048 m		ν_{7H} (doubly degenerate C−H stretching)
3062 vs	3053 m	ν_{2H} (totally symmetric C−H in phase stretching vibration)
3068 m	3069 m	ν_{2H} (totally symmetric C−H in phase stretching vibration)
		$2\nu_{8H}$, $2\nu_{1H} + 2\nu_{6H}$
3161 vw		$2\nu_{8H}$, $2\nu_{1H} + 2\nu_{6H}$

asterisks, are observed at 0.5 GPa, which indicate a transition between phase I and V (their labels will be discussed later). Upon further compression, a new lattice mode at 116 cm^{-1} appearing at 1.7 GPa evidences another transition, from phase V to VI. At 3.7 GPa, the dependence of lattice modes on pressure is clearly discontinuous, and a new peak is found at 181 cm^{-1}, which indicates the transition from phase VI to VII (Figure 1b). The fourth phase transition (VII to VIII) is evidenced by the emergence of the new lattice modes at 108 and 247 cm^{-1} at 11.3 and 14.2 GPa, respectively. Combining with the variations of the internal modes, IR spectra, and XRD results described below, five phases (I, V, VI, VII, VIII) of $C_6H_6{-}C_6F_6$ cocrystal have been identified under high pressure with the transition boundaries at 0.5, 1.7, 3.7, and 11.3 GPa, respectively (Figure 2c).

Internal modes provide the information about the local variations of the chemical environment around specific groups. At 0.8 GPa, both the ν_{7H} and ν_{2H} become doublet, corresponding to the phase transition from I to V (Figure 3e). Meanwhile, a peak at ∼705 cm^{-1} comes out, originated from out-of-plane motion of benzene ring (ν_{4H}) (Figure 3b).[34] At 1.7 GPa, a shoulder band at ∼388 cm^{-1} is observed at the high-frequency side of CF out-of-phase bending mode (ν_{10F}), which becomes a separated peak upon compression (Figure 3a). Simultaneously, the CH in-plane bending mode (ν_{9H}, ∼1170 cm^{-1}) splits, similar to the case of benzene, which implies that the planar motion of benzene ring is degenerated (Figure 3d). These are attributed to the transition from phase V to VI. At the transition from phase VI to VII above 3.7 GPa, ν_{2H} and ν_{7H} (3000−3100 cm^{-1}) split (Figure 3e); five new peaks emerge at 465, 714, 1008, 1203, and 1598 cm^{-1} (Figure 3a−d), respectively. At the phase transition from VII to VIII around 13 GPa, the peak at 1598 cm^{-1} (ν_{8H}) splits again (Figure 3d), a new peak at 613 cm^{-1} emerges in the lower frequency region of ν_{6H} (Figure 3b), and the split branch of ν_{7H} (∼3100 cm^{-1}) depletes at this pressure (Figure 3e). The pressure-dependent Raman modes are summarized in Figure S1, where the variations can be clearly observed and hence the phase transitions are further confirmed.

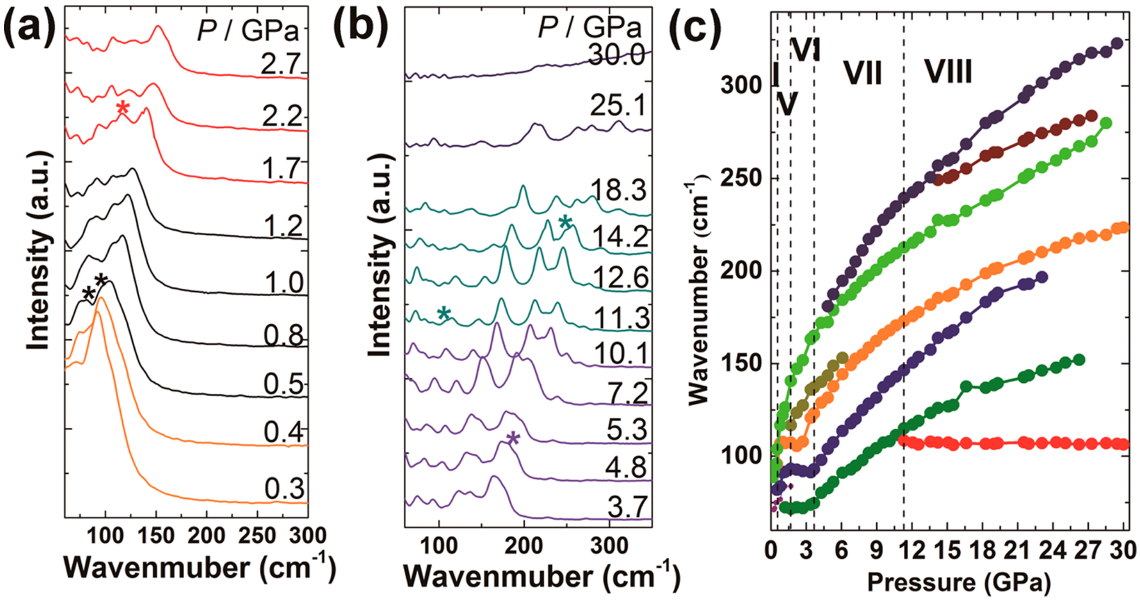

Figure 2. Selected Raman spectra of $C_6H_6{-}C_6F_6$ in the lattice modes region under pressure varying from (a) 0.3 to 2.7 GPa and (b) 3.7 to 30.0 GPa. (c) Frequency shifts of the lattice modes as a function of pressure. The vertical line represents the boundaries of the different phases. The new peaks after phase transitions are marked by the asterisks. The dotted lines represent the phase boundaries.

DOI: 10.1021/acs.jpcc.6b11245
J. Phys. Chem. C 2016, 120, 29510−29519

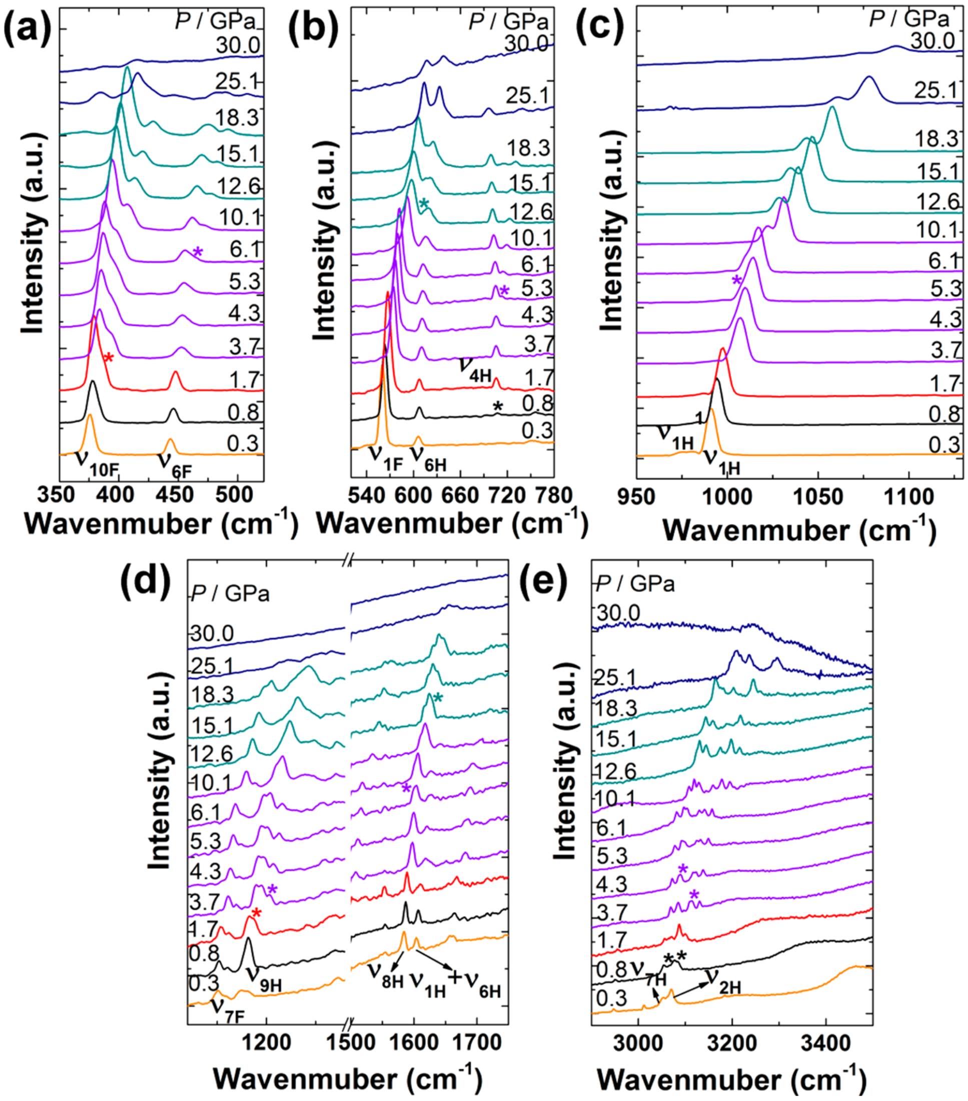

Figure 3. Raman spectral regions of compressed $C_6H_6-C_6F_6$ cocrystal: (a) 350−520, (b) 520−780, (c) 950−1130, (d) 1120−1750, and (e) 2900−3500 cm^{-1} at selected pressures. The omitted ranges of 780−950 and 1750−2900 cm^{-1} lacked fundamental vibrational modes, and that of 1280−1500 cm^{-1} overlapped with the diamond modes. The new peaks after phase transitions are marked by the asterisks.

To understand the interactions between molecules C_6H_6 and C_6F_6 from the Raman spectra, we made a comparison between $C_6H_6-C_6F_6$ cocrystal and its components, pure C_6H_6[34] and C_6F_6.[35] One marked difference is that most of the internal modes of C_6H_6 molecule exhibit varieties at higher pressures in the $C_6H_6-C_6F_6$ cocrystal. For instance, the in-plane C−C−C bending mode (ν_{6H}) of pure C_6H_6 splits at 1.4 GPa, while for the $C_6H_6-C_6F_6$ cocrystal it splits at 12.7 GPa. In addition, the ring breathing mode of C_6F_6 (ν_{1F}) in $C_6H_6-C_6F_6$ cocrystal is relatively softer than those in pure C_6F_6 and pure C_6H_6. As shown in Figure S2, the slopes of ν_{1F} against pressure are 4.10, 4.07, 2.68, and 1.25 cm^{-1}/GPa in phases V, VI, VII, and VIII, respectively. In contrast, the ring breathing mode in pure C_6F_6 is much higher, at the rates of 8.04, 5.62, 2.78, and 2.69 cm^{-1}/GPa in the corresponding pressure ranges. These features uncovered by Raman spectroscopy are probably related to the different sizes of C_6H_6 and C_6F_6 and the interactions between C_6H_6 and C_6F_6, which are stacked in a different way compared with the pure C_6H_6 and C_6F_6. The main interaction in the cocrystal is the electrostatic interaction between the C_6H_6 and C_6F_6,[22,23,36] while CH⋯π and CF⋯π/CF⋯F contacts dominate the cohesion in pure C_6H_6 and C_6F_6.[13,37−39] The details are still under investigation.

Mid-IR Spectra of $C_6H_6-C_6F_6$ Cocrystal under Compression. Above 25 GPa, most of Raman peaks disappear because of the enhanced fluorescence signal from the polymeric product. To investigate the reaction process, in situ IR spectra were measured under pressure up to 35.1 GPa. The assignments of the IR modes are shown in Table 2 based on the spectrum collected at 77 K and ambient pressure.[33] The phase transitions between phases V, VI, VII, and VIII are clearly identified (Figure 4 and Figure S3). Above 2.3 GPa, a new peak is observed at the low-frequency side of CH wag vibration (ν_{11H}, ∼720 cm^{-1}), and a new peak at 1156 cm^{-1} is also detected (Figure 4a), corresponding to the transition from phase V to VI. Above 3.8 GPa, the combination peak ($\nu_{4F} + \nu_{12F}$, ∼1320 cm^{-1}) splits and a new peak emerges at 3127 cm^{-1}, which is attributed to the transition to phase VII (Figure 4b,c). The transition from phase VII to VIII is evidenced by two features. First, at the high-frequency region of the CH wag vibration (ν_{11H}) and C═C stretching mode (ν_{19H}), as well as in the region of the C−H stretching, three new peaks emerged at

Table 2. Assignments of IR Frequencies of Solid-Phase C_6H_6–C_6F_6 Adduct at 77 K/0.1 MPa[33] and 293 K/0.4 GPa

77 K	0.4 GPa	assignments
685 vvs, 706 m	686.7 s	$\nu\nu_{11H}$ (out-of-plane C–H vibration)
974 m, 980 m		$\nu\nu_{17H}$ (out-of-plane C–H vibration)
993 vvs	990 vvs	$\nu\nu_{20F}$ (C–F stretching)
1016 vvs	1019 vvs	$\nu\nu_{3F} + \nu_{18F}$
1034 vs, 1038 vs	1035 m	$\nu\nu_{18H}$ (C–H deformation vibration)
1045 w	1048 vw	$\nu\nu_{6F} + \nu_{16F}$
1142 vw		$\nu\nu_{15H}$ (C–H deformation vibration)
1147 w		
1311 vw		$\nu\nu_{14H}$ (C=C stretching)
1328 vw		$\nu\nu_{13F}$ (C–F trigonal stretching)
1345 m		$\nu\nu_{4F} + \nu_{12\ F}$
1403 w,1414 w	1404 vw	$\nu\nu_{5H} + \nu_{16\ H}$
1435 w	1438 vw	$\nu\nu_{6F} + \nu_{20F}$
1460 w	1463w	$\nu\nu_{7F} + \nu_{18F}$
1469 m,1479 vvs	1479 s	$\nu\nu_{19H}$ (C–C stretching)
1493 vw		$\nu\nu_{5F} + \nu_{14F}$
1531 vvs	1532vvs	$\nu\nu_{19F}$ (C–C stretching)
1550 s	1554s	$\nu\nu_{10H} + \nu_{11H}$
1574 w		$\nu\nu_{1F} + \nu_{3F} + \nu_{18F}$
		$\nu\nu_{5F} + \nu_{13F}$
1591 w	1592	$\nu\nu_{9F} + \nu_{13F}$
1618 vw, 1685 vw		unassigned in C_6H_6
1754 w	1757 w	$\nu\nu_{7F} + \nu_{16F}$
1807 vw	1807w	$\nu\nu_{1F} + \nu_{14F}$
1833 m	1830 w	$\nu\nu_{10H} + \nu_{17H}$
1975 m		$\nu\nu_{5H} + \nu_{17H}$
2089 w, 2094 vw		$\nu\nu_{1F} + \nu_{19F}$
2144 vw		$\nu\nu_{7F} + \nu_{20F}$
2262 vw		$\nu\nu_{8F} + \nu_{16F}$
2329 vw		unassigned in C_6H_6
2469 vw, 2474 vw	2469 w	$\nu\nu_{7F} + \nu_{13F}$
2505 vw	2505 vw	$\nu\nu_{2F} + \nu_{3F} + \nu_{18F}$
2656 vw	2656 vw	$\nu\nu_{8F} + \nu_{20F}$
2682 w	2682 w	$\nu\nu_{7F} + \nu_{19F}$
2817 vw		unassigned in C_6H_6
2983 vw	2983 vw	$\nu\nu_{8F} + \nu_{13F}$
3005 vw		$\nu\nu_{3F} + \nu_{8F} + \nu_{12F}$
3024 vw	3019 w	$\nu\nu_{2F} + \nu_{19F}$
3030 s, 3037 s	3040 m	$\nu\nu_{20H}$ (C–H stretching)
3068 m	3074 m	$\nu\nu_{13H}$ (C–H stretching)
3086 s, 3091 m	3094 m	$\nu\nu_{8H} + \nu_{19H}$

723, 1514, and 3228 cm^{-1} above 10 GPa. Second, the C–H deformation vibration (ν_{18H}), the combination peak ($\nu_{4F} + \nu_{12F}$), and the peak next to $\nu_{8H} + \nu_{19H}$ mode split. Notably, the red shift is observed for the combination peak ($\nu_{4F} + \nu_{12F}$) at 1345 cm^{-1} and also for the new peak (1336 cm^{-1}) emerged above 3.8 GPa (Figure S3b). The reason is still under investigation.

At 25 GPa, a very broad peak is observed at 1370 cm^{-1} (Figure 4b), which indicates the starting of the chemical reaction. The peak is dramatically enhanced upon further compression, and several new peaks around 798, 844, 955, 1159, and 1855 cm^{-1} (marked by the blue dots) are detected. Above 28 GPa, the C–H stretching around 3000 cm^{-1} is significantly broadened and weakened, followed by the remaining peaks of C_6F_6–C_6H_6 cocrystal. When the sample is compressed to 30–35 GPa, almost all of the peaks from the C_6F_6–C_6H_6 cocrystal disappear, and the new peaks around 966, 1179, 1388, 2648, and 3311 cm^{-1} are attributed to the polymeric product (marked by the blue dots).

Figure 5 shows the infrared spectra of C_6F_6–C_6H_6 cocrystal under decompression. It demonstrates that the pressure-induced polymerization is irreversible. The solid polymer recovered from 35 GPa is a white sample, similar to PIP-B.[40] As shown in Figure 5b, the peaks in the region of the 842–958, 1312, and 2910 cm^{-1} correspond to C(sp^3)–H wagging, *trans*-C–H symmetrical rocking, and C(sp^3)–H stretching vibrations, respectively, by comparison with the IR spectrum of PIP-B. The additional strong absorption at 1030 and 1106 cm^{-1} should be attributed to vibrations related to fluorine. Taking the case of polyvinyl fluoride (PVF) as reference,[41] the two bands are assigned to C–F and C–C stretching, respectively. The emergence of the peaks at 1030 and 2910 cm^{-1} clearly evidences the polymerization of the cocrystal under high pressure, with a part of C(sp^2) converting into C(sp^3). In addition, we could deduce that sp^2 carbons still exist in the polymer product from the presence of C=C, =C–H, and =C–F stretching bands.

Structure Analysis of C_6H_6–C_6F_6 Cocrystal under Compression. Crystal structure is the key point to understand the phase transitions and the interactions. To determine the crystal structures of the high-pressure phases, we attempted to obtain single crystals of high-pressure phases by controlling the pressure and temperature conditions. Solidified mixture of a C_6H_6–C_6F_6 adduct was melted and as a liquid was loaded to a warm DAC chamber. Single crystals of phases I and V were grown under isochoric conditions by in situ recrystallization of 1:1 C_6H_6 and C_6F_6 mixture. Initially, pressure was increased to 0.13 GPa and a polycrystalline mass was heated, until a single grain was obtained at 408 K (Figure 6). In the next step, a single crystal was grown by cooling the DAC to room temperature. The single crystal of phase V was grown at 0.48 GPa. The mixture was heated to 404 K and subsequently gradually cooled until the crystals filled the chamber's volume. Table 3 lists the details of the structural refinements and crystal data under selected pressures. The crystal structure measured below 0.4 GPa at room temperature shows that it is phase I.[25] The C_6H_6 and C_6F_6 molecules are alternatively stacked to form columns, which, in turn, are arranged into a hexagonal matrix. At 0.5 GPa, phase I transforms to phase V, with the space group transforming from *R*-3*m* to *P*2_1/*c* and abrupt changes of molecular volume and unit cell parameters (Figure S4.).

Because of the data quality, we could not solve the crystal structure of phase V and turned to in situ powder diffraction (shown in Figure 7). Consistently with the Raman and IR experiments, phase transitions V–VI–VII–VIII and a final irreversible amorphization transition were identified. The transition boundary is a bit different from the one observed by the Raman results, which might be due to nonhydrostaticity or the technique itself. The Raman results reflect the evolution of the local structure, while the XRD is related to the long-range ordering. The XRD pattern of phase VI is significantly different from that of phase V. However, what really distinguishes phase VII from phase VI is only the peak around 3° (marked by the asterisk). This implies the structure of phase VII is very similar to phase VI, probably a superstructure. In the pressure range of phase VIII, most of XRD peaks are broadened and finally disappear in the background, which suggests disorder and reactions of molecules. From the patterns we can conclude that the high-pressure phases (V, VI, VII, and VIII) and low-temperature phases (II, III, IV[25]) are different

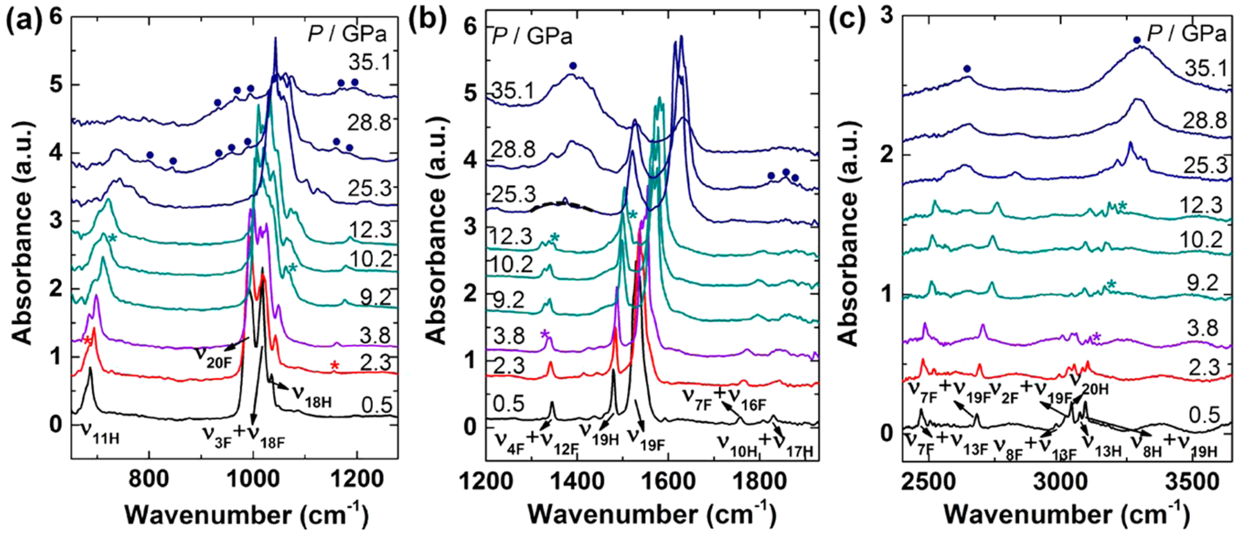

Figure 4. In situ IR spectra of $C_6H_6-C_6F_6$ upon compression in the spectral region of (a) 650−1280, (b) 1200−1930, and (c) 2400−3650 cm^{-1}. The spectral range of 1930−2400 cm^{-1} is omitted due to the strong absorbance of the diamond. The new peaks after phase transitions are marked by the asterisks. The blue dots represent the new peaks after polymerization.

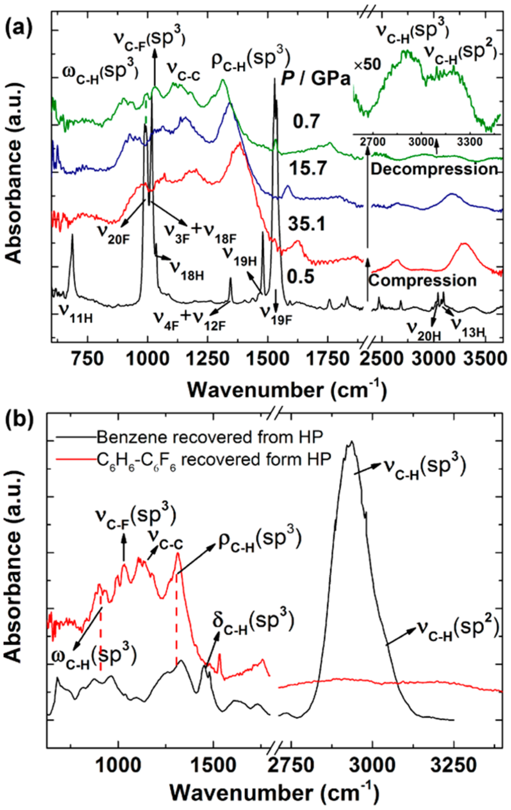

Figure 5. (a) IR spectra of $C_6H_6-C_6F_6$ cocrystal upon compression and decompression at selected pressures. (b) IR spectrum of the $C_6H_6-C_6F_6$ sample and reported C_6H_6 sample recovered from high pressure (HP) (reproduced from ref 40). The IR mode abbreviations are C−H wagging (ω_{C-H}), C−F stretching (ν_{C-F}), C−C stretching (ν_{C-C}), *trans*-C−H symmetrical rocking (ρ_{C-H}), CH_2 bending (δ_{C-H}), and C−H stretching (ν_{C-H}).

from each other (Figure S5), and the phase transitions under different pressure and temperature conditions has been outlined in Figure 8.

The powder sample of phase V has very good crystallinity, and we successfully indexed its powder XRD pattern collected at 1.0 GPa. The lattice parameters are a = 7.6545(6) Å, b = 6.0823(7) Å, c = 11.687(2) Å, and β = 102.498(8)°, which is in good consistence with the single-crystal diffraction data. To determine the atomic positions, rigid bodies of C_6H_6 and C_6F_6 were used. Nine parameters were refined in the final Rietveld refinement, including three rotation degree of freedom for C_6H_6 molecule and three for C_6F_6, scale, preferred orientation, and absorption. The bond lengths of C−C, C−H and C−F are restrained between certain reasonable values. After such a series of crystallographic analysis and tests, the best structure model was found and Rietveld refinement was performed (Figure S6). The crystallographic data and the atomic positions of phase V are listed in Tables 4 and 5, respectively, and the structure model is shown in Figure 9a. The C_6H_6 and C_6F_6 molecules are still alternately packed and form columns; however, the molecules are not straightly stacked but severely tilted.

Taking phase I, IV, and V for comparison, we can find that all of them are constructed by $C_6H_6-C_6F_6$ columns, and the columns are closely (approximately hexagonally) packed (Figure 9a−c). If we define the lattice parameters of phase I as $\mathbf{a}_I$, $\mathbf{b}_I$, and $\mathbf{c}_I$, the lattices of phase IV and V are evolved from $\mathbf{a}_I$, $1/3\mathbf{a}_I + 2/3\mathbf{b}_I + 2/3\mathbf{c}_I$, $\mathbf{c}_I$, with different α, β, and γ angles (Figure 9d). A significant difference between the phases is that in phase I the C_6H_6 and the C_6F_6 planes are perfectly perpendicular to the direction of the column (straightly stacked), while in phases IV and V, they are significantly tilted (Figure 9a−c). In phase IV, all of the molecules tilt toward the same direction and are hence parallel. In phase V, the molecules at (x, 0, 0) and (x, 0.5, 0.5) tilt toward different directions, with a dihedral angle of ∼60°. It is widely recognized that at low temperature the rotations and vibrations of molecules are weakened, which often results in a lower symmetry. Here we can arguably say that the applied pressure of 0.5 GPa (phase V) makes a similar effect on the packing of molecules compared with cooling to ∼200 K (phase IV). This also suggests that under higher pressure in phases VI, VII, and VIII, the molecules are highly restrained and pack in a more distorted way, and the role of $\pi-\pi$ stacking as the dominating cohesion force is considerably reduced.

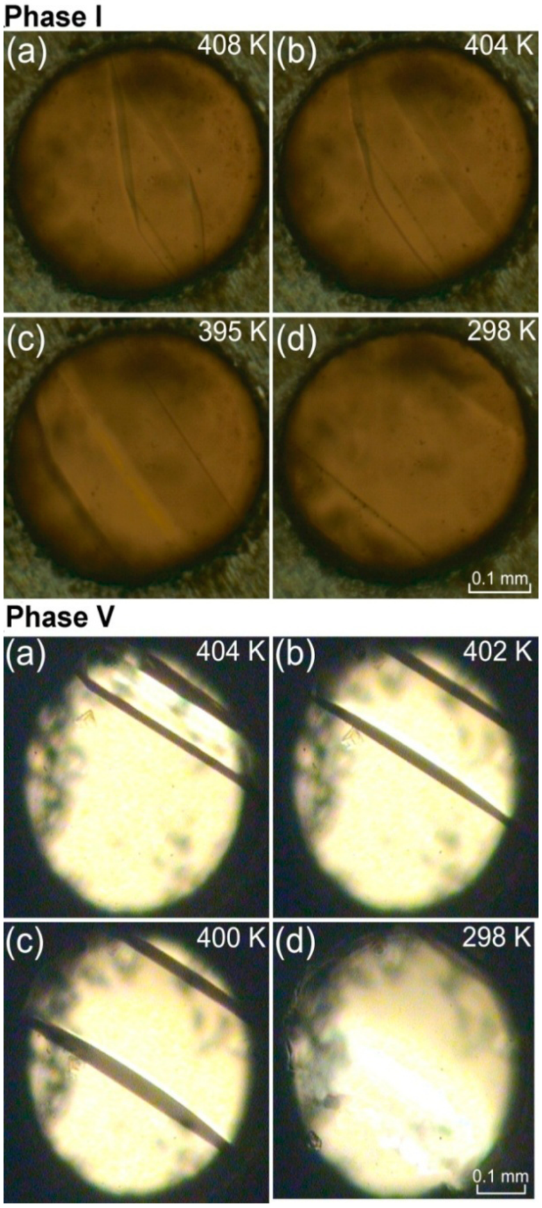

Figure 6. Isochoric growth of C_6H_6−C_6F_6 single crystals of phases I and V at 0.13 and 0.48 GPa, respectively. The high-pressure chambers are fully filled by the crystals at 298 K.

Table 3. Crystallographic Data for Phases I and V of C_6H_6−C_6F_6 Cocrystal under Selected Pressures at 296 K

phase	I	V
formula weight	264.17	264.17
pressure (GPa)	0.35	1.3
wavelength (Å)	0.71073	0.71073
space group	*R*-3*m*	$P2_1/c$
a (Å)	11.924(3)	7.752(18)
b (Å)	11.924(3)	6.1053(5)
c (Å)	7.195(2)	11.763(3)
α (deg)	90	90
β (deg)	90	102.61(9)
γ (deg)	120	90
volume (Å^3)	886.0(4)	543.3(12)
Z	3	2
density (g/cm^3)	1.485	1.615

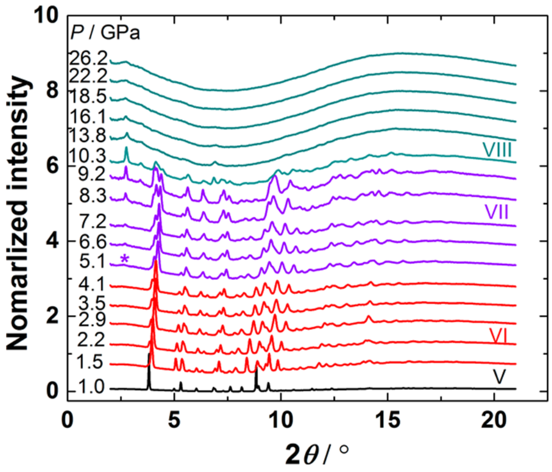

Figure 7. Selected powder XRD patterns of C_6H_6−C_6F_6 cocrystal under high pressure. The new peak after the transition to phase VII is marked by the asterisk.

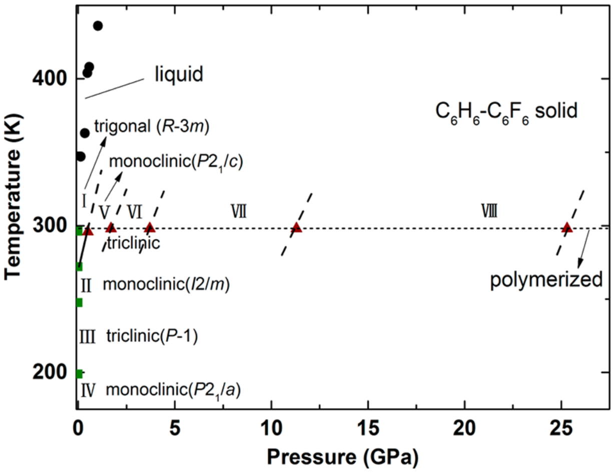

Figure 8. Pressure-induced phase transformations of C_6H_6−C_6F_6 cocrystal at room temperature and the structural phase transitions at ambient pressure and low temperature. The phase boundaries indicated by dashed curves are only speculative.

It is worth paying attention to the fact that in phases IV and V the C_6F_6 and C_6H_6 molecules form 2D layers and bands across the columns, respectively. The nearest H···F distances are 2.5 to 2.7 Å in the layers of phase IV and ∼2.2 Å within and between the bands in phase V (Figure S7). This suggests that in phase IV there is a very weak CH···F hydrogen bond and in phase V the CH···F bond is much stronger. According to our previous research of CH_3CN, the hydrogen bond can play important roles in the stacking of molecules as well as in the following chemical reactions under higher pressure.[42]

The diffraction peaks of phase VI above 1.7 GPa are broader and overlapped. The diffraction pattern collected at 3.5 GPa can be indexed as $a = 7.0245(4)$ Å, $b = 9.910(3)$ Å, $c = 7.594(1)$ Å, $\alpha = 105.97(2)°$, $\beta = 99.42(2)°$, and $\gamma = 87.97(2)°$. The decreased data quality considerably hampers the determination of the crystal structure. To explore the crystal structure of phase VI and above, we have employed in situ neutron diffraction measurement of the C_6D_6−C_6F_6 cocrystal at around 1.5, 3.0, 7.0, 12.0, 15.0, and 20.0 GPa (Figure S8). During the whole compressing process, the sample was good powder crystal, as demonstrated by the 2D detector images.

Table 4. Experimental Information of the X-ray Diffraction Data, Crystallographic Data, and Results of Rietveld Analysis for C_6H_6−C_6F_6 Cocrystal Phase V (298 K, 1.02 GPa)

phase	V
chemical formula	$C_6H_6C_6F_6$
M_r (g·mol^{-1})	264.17
space group (number)	$P2_1/c$ (14)
lattice parameters (Å, deg)	a = 7.6545(6), b = 6.0823(7), c = 11.687(2), β = 102.498(8)
V (Å^3)	531.2(1)
Z	2
D_x (g cm^{-3})	1.65
radiation type	synchrotron X-ray
wavelength (Å)	0.4973
diffractometer	BL-12.2.2, Advanced Light Source, Lawrence Berkeley National Lab
data collection method	Debye−Scherrer geometry
specimen mounting	diamond anvil cell
detector	image plate
data collection mode	transmission
R_p, R_{wp}	0.967, 1.442
number of data points	2413
number of parameters	9
computer program	TOPAS-3

Table 5. Atomic Coordinates for C_6H_6−C_6F_6 Cocrystal at (298 K, 1.02 GPa)

atom	x	y	z
C1	0.0843	0.1824	−0.0244
C2	−0.0809	−0.1333	−0.0873
C3	0.0034	0.0491	−0.1117
C4	0.5935	0.1015	0.0962
C5	0.5299	−0.1027	0.1043
C6	0.4364	−0.2042	0.0082
F1	0.6901	0.2063	0.1955
F2	0.5608	−0.2088	0.2121
F3	0.3707	−0.4151	0.0166
H1	0.1630	0.3526	−0.0471
H2	−0.1564	−0.2577	−0.1688
H3	0.0066	0.0950	−0.2159

[a] All site occupancies were equal to 1.0 and the temperature factors (B) of all atoms were set to 1 Å^2.

Because of the error of the pressure loading curve, the pressure could not be precisely controlled. Phases I and V were hence missed, and the first phase observed is phase VI, which can be perfectly fitted using the lattice parameters mentioned above. The neutron diffraction patterns show obvious differences between 7.0 and 12.0 GPa, consistently with the phase transition from phase VII to VIII. However, the VI−VII phase transition is not obvious in the *d*-range measured, which indicates that it is a minor phase transition. The diffraction peaks of phase VIII still resemble those of phases VII and VI to some extent, which implies the similarities between their structures, as explained above.

■ CONCLUSIONS

Structure evolution of C_6H_6−C_6F_6 cocrystal was investigated under high pressure at ambient temperature using in situ Raman, mid-IR spectroscopy, X-ray diffraction, and neutron diffraction. Four molecular phase transitions at ~0.5, 1.7, 3.7, and 11.3 GPa and the polymerization have been determined and phase V−VIII are hence identified. XRD and neutron diffraction studies show that these phases are different from phases II, III, and VI reported at low temperature.[25] Among them, phase V has a tilted column structure, which suggests that the π−π stacking dominating the molecular aggregation at low pressure becomes less significant under extreme compression. Phase VIII polymerizes above 25 GPa irreversibly, producing an amorphous sp^3(CH/F)$_n$ material. Our work evidences the PIP of C_6H_6−C_6F_6 cocrystal, figures out the phase behaviors before the PIP, and hence provides necessary information to understand the PIP of C_6H_6−C_6F_6 cocrystal. This work also provides important reference for the high-pressure research on C_6H_6−C_6F_6-based supramolecules.

■ ASSOCIATED CONTENT

Supporting Information

The Supporting Information is available free of charge on the ACS Publications website at DOI: 10.1021/acs.jpcc.6b11245.

> Figure S1. Pressure dependences of the internal Raman frequencies of C_6H_6−C_6F_6 cocrystal at room temperature. Figure S2. Linear simulation results of ν_{1F} (ring breathing mode) in C_6H_6−C_6F_6 cocrystal and in C_6F_6. Figure S3. Pressure dependences of IR-active modes of C_6H_6−C_6F_6 cocrystal at ambient temperature. Figure S4. Molecular volume and unit-cell dimensions of phases I and V of C_6H_6−C_6F_6 cocrystal as a function of pressure. Figure S5. X-ray diffraction patterns of phases II and III of C_6H_6−C_6F_6 cocrystal. Figure S6. Retrieved refinement plot of C_6H_6−C_6F_6 cocrystal in phase V. Figure S7. The H···F distances in phases IV and V of C_6H_6−C_6F_6 cocrystal. Figure S8. In situ neutron diffraction measurement of the C_6D_6−C_6F_6 cocrystal at 1.5, 3.0, 7.0, 12.0, 15.0, and 20.0 GPa. (PDF)

■ AUTHOR INFORMATION

Corresponding Authors

*H.Z.: E-mail: zhenghy@hpstar.ac.cn.
*K.L.: E-mail: likuo@hpstar.ac.cn.

ORCID

Haiyan Zheng: 0000-0002-4727-5912
Andrzej Katrusiak: 0000-0002-1439-7278

Author Contributions

All authors have given approval to the final version of the manuscript.

Notes

The authors declare no competing financial interest.

■ ACKNOWLEDGMENTS

We acknowledge the support of NSAF (Grant No. U1530402) and National Natural Science Foundation of China (NSFC) (Grant Nos. 21601007 and 21501162). Use of Advanced Light Source (ALS) is supported by the Director, Office of Science, Office of Basic Energy Sciences, of the U.S. Department of Energy under Contract No. DE-AC02-05CH11231. Neutron diffraction experiments were performed through the J-PARC user programs (No. 2016A0191).

■ REFERENCES

(1) Jariwala, D.; Sangwan, V. K.; Lauhon, L. J.; Marks, T. J.; Hersam, M. C. Carbon Nanomaterials for Electronics, Optoelectronics, Photovoltaics, and Sensing. *Chem. Soc. Rev.* **2013**, *42*, 2824−2860.

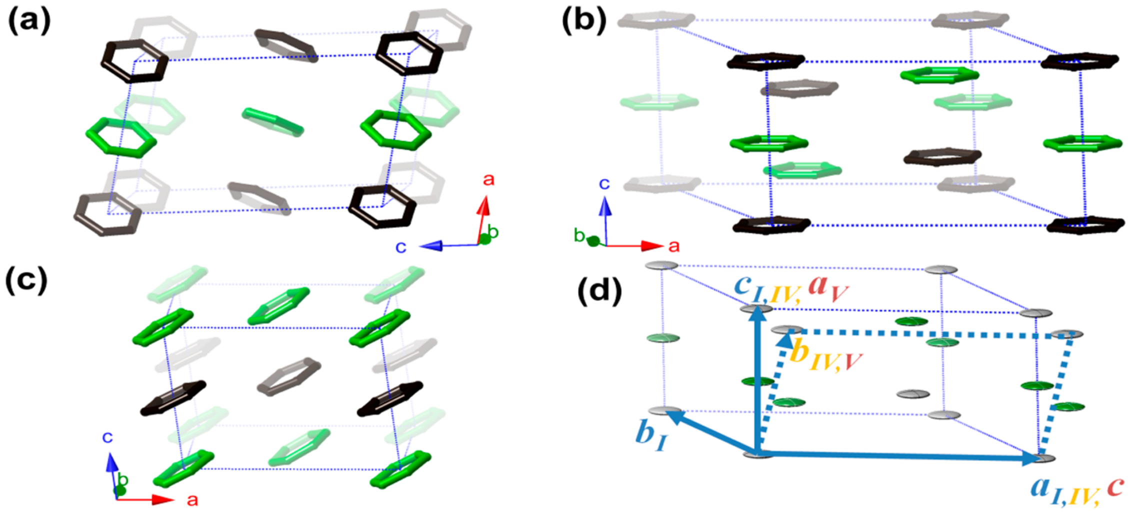

Figure 9. Crystal structure of C_6H_6−C_6F_6 cocrystal (a) phase V, (b) phase I, (c) phase IV,[25] and (d) the relationship of the lattices of phases I, IV, and V. The rings in black and green represent molecules C_6H_6 and C_6F_6, respectively.

(2) Tzirakis, M. D.; Orfanopoulos, M. Radical Reactions of Fullerenes: From Synthetic Organic Chemistry to Materials Science and Biology. *Chem. Rev.* **2013**, *113*, 5262−5321.

(3) Feldman, A. K.; Steigerwald, M. L.; Guo, X.; Nuckolls, C. Molecular Electronic Devices Based on Single-Walled Carbon Nanotube Electrodes. *Acc. Chem. Res.* **2008**, *41*, 1731−1741.

(4) Schettino, V.; Bini, R. Chemical Reactions at High Pressure. *Phys. Chem. Chem. Phys.* **2003**, *5*, 1951−1965.

(5) Schettino, V.; Bini, R. Constraining Molecules at the Closest Aapproach: Chemistry at High Pressure. *Chem. Soc. Rev.* **2007**, *36*, 869−880.

(6) McMillan, P. F. Chemistry at High Pressure. *Chem. Soc. Rev.* **2006**, *35*, 855−857.

(7) Bini, R. Laser-Assisted High-Pressure Chemical Reactions. *Acc. Chem. Res.* **2004**, *37*, 95−101.

(8) Aoki, K.; Usuba, S.; Yoshida, M.; Kakudate, Y.; Tanaka, K.; Fujiwara, S. Raman Study of the Solid State Polymerization of Acetylene at High Pressure. *J. Chem. Phys.* **1988**, *89*, 529−534.

(9) Li, K.; Zheng, H.; Ivanov, I. N.; Guthrie, M.; Xiao, Y.; Yang, W.; Tulk, C. A.; Zhao, Y.; Mao, H.-k. $K_3Fe(CN)_6$: Pressure-Induced Polymerization and Enhanced Conductivity. *J. Phys. Chem. C* **2013**, *117*, 24174−24180.

(10) Yamawaki, H.; Sakashita, M.; Aoki, K.; Takemura, K. Reversible Phase Transition between the Metastable Phases of Tetracyanoethylene under High Pressure. *Phys. Rev. B: Condens. Matter Mater. Phys.* **1996**, *53*, 11403−11407.

(11) Li, K.; Zheng, H.; Hattori, T.; Sano-Furukawa, A.; Tulk, C. A.; Molaison, J.; Feygenson, M.; Ivanov, I. N.; Yang, W.; Mao, H.-k. Synthesis, Structure, and Pressure-Induced Polymerization of $Li_3Fe(CN)_6$ Accompanied with Enhanced Conductivity. *Inorg. Chem.* **2015**, *54*, 11276−11282.

(12) Ciabini, L.; Gorelli, F. A.; Santoro, M.; Bini, R.; Schettino, V.; Mezouar, M. High-Pressure and High-Temperature Equation of State and Phase Diagram of Solid Benzene. *Phys. Rev. B: Condens. Matter Mater. Phys.* **2005**, *72*, 094108.

(13) Katrusiak, A.; Podsiadło, M.; Budzianowski, A. Association CH···π and No van der Waals Contacts at the Lowest Limits of Crystalline Benzene I and II Stability Regions. *Cryst. Growth Des.* **2010**, *10*, 3461−3465.

(14) Pruzan, P.; Chervin, J. C.; Thiéry, M. M.; Itié, J. P.; Besson, J. M.; Forgerit, J. P.; Revault, M. Transformation of Benzene to a Polymer after Static Pressurization to 30 GPa. *J. Chem. Phys.* **1990**, *92*, 6910−6915.

(15) Ciabini, L.; Santoro, M.; Bini, R.; Schettino, V. High Pressure Reactivity of Solid Benzene Probed by Infrared Spectroscopy. *J. Chem. Phys.* **2002**, *116*, 2928−2935.

(16) Jackson, B. R.; Trout, C. C.; Badding, J. V. UV Raman Analysis of the C:H Network Formed by Compression of Benzene. *Chem. Mater.* **2003**, *15*, 1820−1824.

(17) Engelke, R.; Hay, P. J.; Kleier, D. A.; Wadt, W. R. A Theoretical Study of Possible Benzene Dimerizations under High-Pressure Conditions. *J. Chem. Phys.* **1983**, *79*, 4367−4375.

(18) Citroni, M.; Bini, R.; Foggi, P.; Schettino, V. Role of Excited Electronic States in the High-Pressure Amorphization of Benzene. *Proc. Natl. Acad. Sci. U. S. A.* **2008**, *105*, 7658−7663.

(19) Ciabini, L.; Santoro, M.; Gorelli, F. A.; Bini, R.; Schettino, V.; Raugei, S. Triggering Dynamics of the High-Pressure Benzene Amorphization. *Nat. Mater.* **2007**, *6*, 39−43.

(20) Ciabini, L.; Santoro, M.; Bini, R.; Schettino, V. High Pressure Photoinduced Ring Opening of Benzene. *Phys. Rev. Lett.* **2002**, *88*, 085505.

(21) Fitzgibbons, T. C.; Guthrie, M.; Xu, E.-s.; Crespi, V. H.; Davidowski, S. K.; Cody, G. D.; Alem, N.; Badding, J. V. Benzene-Derived Carbon Nanothreads. *Nat. Mater.* **2014**, *14*, 43−47.

(22) Patrick, C. R.; Prosser, G. S. A Molecular Complex of Benzene and Hexafluorobenzene. *Nature* **1960**, *187*, 1021.

(23) Williams, J. H. The Molecular Electric Quadrupole Moment and Solid-State Architecture. *Acc. Chem. Res.* **1993**, *26*, 593−598.

(24) Overell, J. S. W.; Pawley, G. S. An X-ray Single-Crystal Study of the Molecular System $C_6F_6.C_6D_6$. *Acta Crystallogr., Sect. B: Struct. Crystallogr. Cryst. Chem.* **1982**, *B38*, 1966−1972.

(25) Williams, J. H.; Cockcroft, J. K.; Fitch, A. N. Structure of the Lowest Temperature Phase of the Solid Benzene-Hexafluorobenzene Adduct. *Angew. Chem., Int. Ed. Engl.* **1992**, *31*, 1655−1657; *Angew. Chem.* **1992**, *104*, 1666−1669.

(26) Cavallo, G.; Metrangolo, P.; Milani, R.; Pilati, T.; Priimagi, A.; Resnati, G.; Terraneo, G. The Halogen Bond. *Chem. Rev.* **2016**, *116*, 2478−2601.

(27) Kim, K.; An, T. K.; Kim, J.; Jeong, Y. J.; Jang, J.; Kim, H.; Baek, J. Y.; Kim, Y.-H.; Kim, S. H.; Park, C. E. Grafting Fluorinated Polymer Nanolayer for Advancing the Electrical Stability of Organic Field-Effect Transistors. *Chem. Mater.* **2014**, *26*, 6467−6476.

(28) Zhao, J.; Zhou, T.; Zhang, J.; Chen, H.; Yuan, C.; Zhang, W.; Zhang, A. Synthesis of a Waterborne Polyurethane-Fluorinated Emulsion and Its Hydrophobic Properties of Coating Films. *Ind. Eng. Chem. Res.* **2014**, *53*, 19257−19264.

(29) Mao, H.-k.; Xu, J.; Bell, P. M. Calibration of the Ruby Pressure Gauge to 800 kbar under Quasi-Hydrostatic Conditions. *J. Geophys. Res.* **1986**, *91*, 4673−4676.

(30) Prescher, C.; Prakapenka, V. B. DIOPTAS: a Program for Reduction of Two-Dimensional X-ray Diffraction Data and Data Exploration. *High Pressure Res.* **2015**, *35*, 223−230.

(31) Hattori, T.; Sano-Furukawa, A.; Arima, H.; Komatsu, K.; Yamada, A.; Inamura, Y.; Nakatani, T.; Seto, Y.; Nagai, T.; Utsumi, W.; et al. Design and Performance of High-Pressure PLANET Beamline at Pulsed Neutron Source at J-PARC. *Nucl. Instrum. Methods Phys. Res., Sect. A* **2015**, *780*, 55−67.

(32) Budzianowski, A.; Katrusiak, A. *High-Pressure Crystallography*; Kluwer Academic Publishers: Dordrecht, The Netherlands, 2004; pp 101−112.

(33) Laposa, J. D.; Mcglinchey, M. J.; Montgomery, C. Infrared and Raman Spectra of $C_6H_6C_6F_6$. *Spectrochim. Acta* **1983**, *39A*, 863−866.

(34) Thiéry, M.; Léger, J. High Pressure Solid Phases of Benzene. I. Raman and X-Ray Studies of C_6H_6 at 294 K up to 25 GPa. *J. Chem. Phys.* **1988**, *89*, 4255−4271.

(35) Pravica, M.; Sneed, D.; Wang, Y.; Smith, Q.; White, M. Hexafluorobenzene under Extreme Conditions. *J. Phys. Chem. B* **2016**, *120*, 2854−2858.

(36) Dahl, T.; Niinistö, L.; Møller, J.; Schroll, G.; Leander, K.; Swahn, C.-G. Crystal Structure of the Triclinic Form of the 1:1 Complex between Hexamethylbenzene and Hexafluorobenzene at −40 Degrees C. *Acta Chem. Scand.* **1973**, *27*, 995−1003.

(37) Budzianowski, A.; Katrusiak, A. Pressure-Frozen Benzene I Revisited. *Acta Crystallogr., Sect. B: Struct. Sci.* **2006**, *B62*, 94−101.

(38) Boden, N.; Davis, P. P.; Stam, C. H.; Wesselink, G. A. Solid Hexafluorobenzene. *Mol. Phys.* **1973**, *25*, 81−86.

(39) Shorafa, H.; Mollenhauer, D.; Paulus, B.; Seppelt, K. The Two Structures of the Hexafluorobenzene Radical Cation $C_6F_6(^{\bullet+})$. *Angew. Chem., Int. Ed.* **2009**, *48*, 5845−5847; *Angew. Chem.* **2009**, *121*, 5959−5961.

(40) Ciabini, L.; Santoro, M.; Bini, R.; Schettino, V. High Pressure Reactivity of Solid Benzene Probed by Infrared Spectroscopy. *J. Chem. Phys.* **2002**, *116*, 2928−2934.

(41) Hong, J. W.; Lando, J. B.; Koenig, J. L.; Chough, S. H.; Krimm, S. Normal-Mode Analysis of Infrared and Raman Spectra of Polyhinyl Fluoride. *Vib. Spectrosc.* **1992**, *3*, 55−66.

(42) Zheng, H.; Li, K.; Cody, G. D.; Tulk, C. A.; Dong, X.; Gao, G.; Molaison, J. J.; Liu, Z.; Feygenson, M.; Yang, W.; et al. Polymerization of Acetonitrile via a Hydrogen Transfer Reaction from CH_3 to CN under Extreme Conditions. *Angew. Chem., Int. Ed.* **2016**, *55*, 12040−12044; *Angew. Chem.* **2016**, *128*, 12219−12223.